Implications of simultaneous requirements for low-noise exchange gates in double quantum dots

Erik Nielsen, Ralph W. Young, Richard P. Muller, and M. S. Carroll
Sandia National Laboratories, Albuquerque, New Mexico 87185, USA
(Received 13 April 2010; revised manuscript received 14 July 2010; published 17 August 2010)

Achieving low-error, exchange-interaction operations in quantum dots for quantum computing imposes simultaneous requirements on the exchange energy's dependence on applied voltages. A double quantum dot qubit, approximated with a quadratic potential, is solved using a full configuration interaction method. This method is more accurate than Heitler-London and Hund-Mulliken approaches and captures new and significant qualitative behavior. We show that multiple regimes can be found in which the exchange energy's dependence on the bias voltage between the dots is compatible with current quantum error correction codes and state-of-the-art electronics. Identifying such regimes may prove valuable for the construction and operation of quantum gates that are robust to charge fluctuations, particularly in the case of dynamically corrected gates.

DOI: 10.1103/PhysRevB.82.075319 PACS number(s): 73.21.La, 03.67.Lx

I. INTRODUCTION

A quantum bit (qubit) typically encodes information in a two-level system. The exchange energy between quantum dots was first suggested as sufficient to perform a universal gate set (unitary coherent manipulations of one and two qubits for logical operations) by Levy,[1] and subsequent exchange-based proposals for solid-state architectures have been suggested by Loss-DiVincenzo,[2] Kane,[3] and Taylor.[4] The exchange interaction causes a splitting between quantum states called the *exchange energy*, which we denote J. Qubit rotations are performed experimentally by electrically increasing the exchange energy for short times.[5]

Several important noise sources that can produce error in the exchange operation include charge fluctuations (e.g., random telegraph noise, Johnson and shot noise), inaccuracy in electronics control (e.g., ringing and over/undershoot) and rotations due to inhomogeneous fields.

Quantum error correction (QEC) schemes have been developed to cope with noise and errors in future quantum circuits.[6] A quantum error correction code introduces redundancy in the qubit information providing the ability to correct for errors through majority vote checks on the redundant basis bits.[7] These coding schemes are believed to be a necessary component of any future quantum computer because of the fragile nature of qubits. However, the codes provide benefit only for cases when the qubit gate error rate is less than a threshold value P_{th} above which the error correction circuit is more faulty than a bare qubit. Thresholds have been estimated for a number of cases and almost ubiquitously predict very strict limits on the tolerable error in the gate operations (e.g., $P_{th}=2\times10^{-4}$ and $P_{th}=2\times10^{-5}$ from Refs. 4 and 8).

A number of approaches are being pursued to minimize errors in qubit gates to achieve operations that are sufficient to realize the benefits of quantum error correction codes. The exchange gate couples the charge degree of freedom to the spin degree of freedom, which is useful for electronic control of the spins but also exposes the gate to errors induced by the electrodynamics of the system. A number of strategies have been proposed in the literature to address different forms of errors (e.g., large J for fast rotations relative to noise sources,[1] $dJ/d(\text{bias})\approx0$ to suppress the impact of voltage fluctuations similar to those due to detuning,[9] and multiple rotation velocities for dynamically corrected gating[10]). These strategies introduce a number of constraints, and it is not obvious that all of them can be simultaneously implemented in a double quantum dot (DQD) given the physics of the system. In this paper, we show that the simultaneous constraints are consistent with a semiqualitative model of a double quantum-dot system.

A configuration interaction (CI) method[11] is used to study J as a function of parameters which specify a double quantum-dot system. This CI method is more general than Heitler London (HL), Hund Mulliken (HM), and Hubbard model approaches, and is found invaluable to accurately calculate, in the single-valley case, energies for the bias range approaching and within the regime where there is two-electron occupation of one dot. The two-electron occupancy regime is relatively insensitive to the interdot bias $[dJ/d(\text{bias})\approx0]$, making it an important regime to accurately calculate. Furthermore, this method is less computationally demanding than techniques requiring a large mesh, allowing a tractable search for robust exchange interaction parameters in the double dot system.

We begin by describing our DQD model in Sec. II, and outlining the CI method used to solve it in Sec. III. We then develop in Sec. IV the constraints placed on a DQDs exchange energy by quantum error correction codes and controlling electronics. Results are presented in Sec. V, and analyzed using the noise constraints. Finally, we discuss implications and a complementary approach to noise mitigation in Sec. VI, and end with summary and conclusions in Sec. VII.

II. MODEL

A lateral quantum-dot singlet-triplet qubit qualitatively similar to that described by Taylor *et al.*[4] is examined in this paper. To provide a semiquantitative analysis, we use gallium arsenide material constants $m^*=0.067m_e$ and $\kappa=12.9$. The computational basis (i.e., the "0" and "1" states of the effective two-level system which encodes the quantum information) consists of the two-electron singlet and $S_z=0$ triplet

 ©2010 The American Physical Society

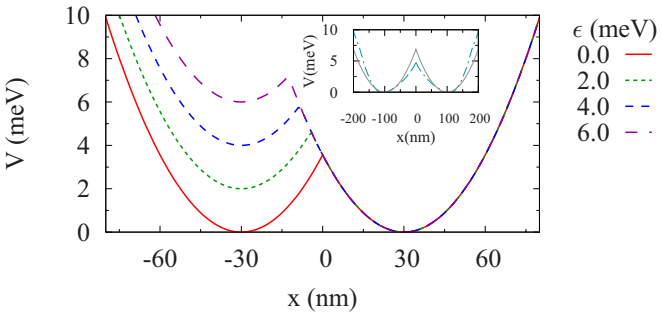

FIG. 1. (Color online) DQD potential along x axis, $V(x,0)$, for $L=30$ nm and $E_0=3.0$ meV. The inset shows the potential obtained by solving Poisson's equation for both electrons and holes using a commercially available solver for an accurate DQD placement of gates and insulators. The dotted line is a double-parabolic potential and shows that a potential of this form is a relatively good approximation to the potentials expected in real devices.

states of lowest energy. J is the splitting between these two states. Note that the triplet states with $S_z=\pm 1$ are split off with a dc magnetic field (typically of order 100 mT). The qubit's effective many-body Hamiltonian is given by

$$\mathcal{H}=\mathcal{H}_1+\mathcal{H}_2+\frac{e^2}{\kappa r_{12}};\quad \mathcal{H}_i=\frac{\vec{P}^2}{2m^*}+V(\vec{r})+\frac{e}{m^*}\vec{S}\cdot\vec{B} \quad (1)$$

where $r_{12}=|\vec{r}_1-\vec{r}_2|$ and κ is the GaAs dielectric constant. In $\mathcal{H}_i$, $\vec{P}=\vec{p}-e\vec{A}$, and $\vec{p}=(p_x,p_y)$ and $\vec{r}=(x,y)$ are the usual momentum and position operators of the i^{th} electron. $\vec{A}$ is a vector potential for the magnetic field $\vec{B}=\vec{\nabla}\times\vec{A}$, and V is the electrostatic potential. A constant perpendicular field $\vec{B}=B\hat{z}$ is considered here, and we restrict ourselves to two dimensions (2D).

The electrostatic potential V is generated by lithographically formed gates near the semiconductor interface. By applying different voltages to these gates at different times, the shape of V and the exchange energy can be tuned to perform operations on the qubit (e.g., see Ref. 5). We idealize V as the minimum of two parabolic dots,

$$V(x,y)=\frac{1}{2}m^*\omega^2[\min((x-L)^2+\epsilon,(x+L)^2)+y^2]. \quad (2)$$

The parameters ϵ, L, and ω, correspond to the bias, interdot distance, and frequency of the ground state as well as a measure of the confining well potential, respectively. One benefit of this parametrization is the ability to vary all three of these aspects independently. Cuts of the 2D potential along the x axis for different ϵ are shown in Fig. 1. This potential has a sharp peak between the dots which we do not expect in an actual device. We have, however, considered the affect of "rounding off" the peak to find that it does not change the semiquantitative results of this work, and therefore choose to continue with the simpler peaked potential of Eq. (2). For later reference, we define the dot size $d=\sqrt{\hbar^2/(m^*E_0)}$ as the width of the ground-state probability distribution in a parabolic well with confinement energy E_0, where $E_0=\hbar\omega$.

III. CALCULATION METHOD

The method used to solve for a system's energies and wave functions follows the standard full CI prescription:[11] Hamiltonian (1) is diagonalized in a many-electron basis formed by taking all possible Slater determinants of a set of single-particle wave functions. The choice of these single-particle functions is crucial to the practical execution of the method, as only a limited (usually quite small) number of them can be used due to the size of the resulting many-electron Hilbert space. As has been done in the past,[12–16] in our approach the single-particle basis wave functions are linear combinations of Gaussian functions. The aim in using such functions is to reduce the basis size needed to accurately model a system while allowing nearly all of the Hamiltonian matrix elements to be computed analytically, which results in a substantial performance advantage over approaches which discretize the system using a dense real-space mesh. Derivations of relevant matrix elements are given in Appendix A Our approach differs from those cited above primarily in the optimization scheme used to choose the Gaussian basis functions. The central piece of this scheme makes use of the fact that the full CI is a variational technique, and minimizes a many-electron state energy.

We now outline the method as a series of steps, referring to the appendices where appropriate. First we construct a set of n_G s-type Gaussian functions where each element g is parametrized by a position (x_g,y_g) and exponential decay coefficient α_g,

$$g(x,y)=Ne^{-\alpha_g(x-x_g)^2}e^{-\alpha_g(y-y_g)^2}e^{ieB/2\hbar(y_0x-x_0y)}. \quad (3)$$

N is a normalization coefficient and B is the magnetic field. The positions of these n_G elements lie in a two-dimensional plane, and their relative (to each other) arrangement is specified as input. Initial values of the absolute positions and exponential decay coefficients of the elements are also given as input. Final values for these parameters are set via the optimization procedure described in Appendix B For the exchange energy values we report, energies for singlet and unpolarized triplet symmetry states are minimized separately and the lowest energy state of each symmetry is used to compute the final exchange energy. Except when otherwise noted, the results presented here optimize an 18-element set of Gaussians (nine on each dot, arranged in a 3×3 grid as shown in Fig. 2) for the singlet and triplet separately.

Once a set of Gaussians has been chosen, whether as part of the optimization procedure or to compute final results, the many-electron energies are computed as follows. The single-particle Hamiltonian, minus the anomalous Zeeman term, is solved using the Gaussian set as a basis. The $n=2n_G$ (including spin degeneracy) resulting single-particle states are taken as an orthonormal (single-particle) basis, and all possible two-particle Slater determinant states are constructed, forming a n_{MB}-dimensional two-particle basis, where $n_{MB}=\binom{n}{2}$. Lastly, the full many-body Hamiltonian is diagonalized in this basis. This method constitutes a full CI with respect to the set of Gaussian functions.

We have performed exchange calculations for different basis sizes and arrangements, and find that for the systems

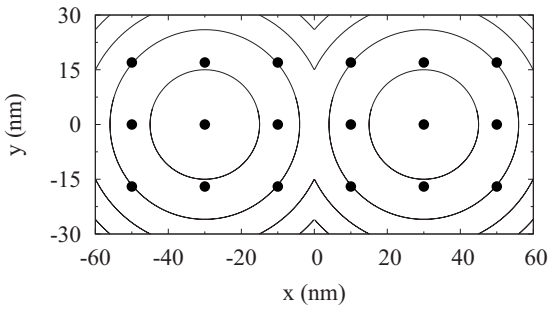

FIG. 2. The relative positions of the Gaussian set elements used in our CI method when $n_G=18$. The center of each Gaussian is marked by a solid circle, and equipotential lines show the dot locations. The nine elements on each dot are arranged in a 3×3 grids which can have different spacings in the x and y direction, as shown. The grid spacings are chosen to minimize the lowest singlet or $S_z=0$ triplet energy, as described in the text.

we study the low-lying energies converge to within several hundredths of a percent by $n_G=29$. To allow for more complete exploration of parameter space, we present results using $n_G=18$ which have energies converged to at least 0.5%. Since the energies typically involved are tens of millielectron volts, discrepancies from the exact result can be of order 50 μeV. This becomes significant when dealing with differences between two nearly equal energies, such as the exchange energy, which can have a magnitude comparable or much less than 50 μeV as we show in Sec. V. In such cases, however, we find the qualitative features and trends of exchange energy curves to be unaffected by this lack of convergence on or below microelectron volt energy scales. Furthermore, in the cases we have considered, the actual error in the exchange energy due to convergence is much less than the worst case value due to error cancellation, and typically on the scale of several microelectron volt. A more detailed study of the CIs convergence, by comparison to exact results for a doubly occupied single dot [similar to the (0,2)-occupation state of a DQD, which is the slowest to converge], is given in Appendix C In summary, though the trends and tunability of the exchange energies we report below can be taken seriously, their magnitudes must be understood as approximate on the scale of several to tens of microelectron volt. Since in a real device the exact form of the potential is unknown and the problem is only approximately two dimensional, we do not expect these results would be quantitatively applicable even if perfectly converged. We draw our conclusions from trends and order-of-magnitude analyses, and at this level the uncertainty due to convergence is unimportant. We emphasize that our results give a more accurate qualitative and semiquantitative picture than previous variational approaches, and are sufficient to resolve whether or not regimes exist which are robust to charge noise. The limitations and shortcomings of methods such as Heitler London and Hund Mulliken are well known,[17,18] and in any case the CI method is variationally more accurate than either (the space of CI "trial" wave functions includes the HL and HM spaces). Figure 3 below compares results of our CI method with Heitler-London and Hund-Mulliken techniques, and also illustrates the convergence of the method by showing the exchange energy resulting from a basis with $n_G=29$. It exemplifies the inability of HL and HM to even qualitatively capture the regime in which one dot is doubly occupied, which is of great interest to us, and shows that the CI convergence is worst in this regime (in this case the uncertainty in J is at most ≈20 μeV due to convergence).

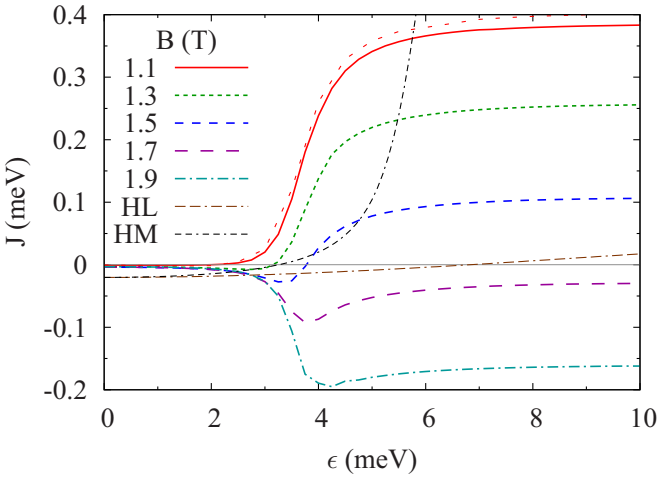

FIG. 3. (Color online) The exchange energy J as a function of interdot bias ϵ for $E_0=3$ meV, $L=30$ nm, and values of the magnetic field around the point where the (0,2) singlet and triplet cross. At large and small ϵ, the curve J is relatively insensitive to changes in ϵ. The transition from positive to negative J in the (0,2) regime (large ϵ) gives rise to a local minimum near $\epsilon=3.5$ meV. This provides a third region where J is relatively robust to ϵ variations. The curves labeled HL and HM show the Heitler London and Hund Mulliken methods for $B=1.1$ T, respectively, and the small dashed curve directly above the solid $B=1.1$ T line shows the $B=1.1$ T result using a larger basis of 29 Gaussian functions.

IV. ERROR ANALYSIS

A. Exchange (rotation) gate

One model of an ideal exchange gate operation is to increase J from (near) zero to a finite value J_1 for a time τ, and then set J back to zero. This rotates the qubit about an angle $\theta=J_1\tau/\hbar$, assuming that the exchange energy is dominant and therefore defines the axis of rotation.

Constraints arise from the error thresholds demanded by error correction codes. In reality J cannot be perfectly controlled, and for an exchange error ΔJ the rotation angle becomes $\theta+\delta$, where $\delta=\Delta J\tau/\hbar$. If J is intended to perform a θ rotation, the gate time $\tau=\hbar\theta/J$, and δ is of order $\Delta J/J$.

The probability of an error during an exchange gate can be estimated as approximately $\cos\delta\approx\delta^2$. The error probability should be engineered to be less than the predicted error threshold P_{th} of the quantum error correction, which was noted earlier to be dependent on the details of the QEC code and have a wide range of projected values (e.g., 10^{-6}–10^{-4}).[4,8] The quantity ΔJ should therefore be targeted to make the ratio $\frac{\Delta J}{J}$ as small as possible such that $(\frac{\Delta J}{J})^2$ is at least smaller than the largest QEC threshold, that is,

$$|\Delta J/J|^2 < P_{th}. \tag{4}$$

The magnitude of J is set by the gate time and target angle of rotation on the Bloch sphere,

$$J = \frac{\hbar\theta}{\tau}. \tag{5}$$

Use of the shortest gate times possible is a common strategy to minimize errors due to time-dependent decoherence mechanisms. Electronics gate speeds are limited by practical considerations (e.g., jitter and control of rise/fall times) and recent analysis suggests gate times in the range of 1–50 ns.[5,8,19] The exchange energy must therefore be of order $1-0.02$ μeV for a $\pi/2$ rotation.

B. No-op (idle) gate

During a no-op gate, when no rotation is desired, J is ideally zero. If instead J takes finite value J_0, an erroneous rotation $\delta_0 = J_0\tau_0/\hbar$ will occur over the time period τ_0. Inserting this into the condition $|\delta_0|^2 < P_{th}$, we find that the the magnitude of the exchange must satisfy

$$|J_0|^2 \leq \hbar^2 P_{th}/\tau_0^2, \tag{6}$$

where τ_0 is length of time the qubit is idle. When $P_{th}=10^{-4}$ this requires $|J_0| \leq 6.5-0.13$ neV for 1–50 ns gate times.

C. Simultaneous constraints

Since an exchange gate operation involves tuning J between two values (usually zero and a finite value J_1), a robust gate requires the existence of at least two *operating points* where Eqs. (4) and (6) are satisfied, respectively, for every needed rotation angle θ.

Additional requirements for dynamically corrected gating (DCG) are also potentially necessary in order to cancel other noise sources such as inhomogeneous quasistatic fields. At least three $J(\epsilon)$ operating points are desired for DCG, and it is useful, but not necessary, for J to be negative at one of them.[10,20] A critical question theoretically is whether the dependence of J on the quantum-dot properties can simultaneously realize several or all of these needs and thereby come closer to fulfilling the strict gate error requirements suggested by present error correction strategies.

V. EXCHANGE ENERGY RESULTS

The dependence of J on the electrostatic potential and magnetic field is examined using the CI method to identify whether the predicted DQD exchange energy can meet the anticipated requirements for an exchange gate. We briefly consider the typical behavior of the exchange energy as a function of system parameters and then we analyze specific noise-robust regimes in detail.

A. Typical behavior

Figure 3 shows the behavior of J as a function of ϵ for varying perpendicular magnetic field strengths. When $B \leq 1.1$ T, the curve has two relatively flat sections at small and large ϵ, where both the singlet and triplet states are in the (1,1) or (0,2) charge sector, respectively. When the interdot barrier is large enough, the quantum states of the DQD will often have an integral number of electrons in each dot. When there are n_L and n_R electrons in the left and right dots, respectively, the state is said to be in the (n_L,n_R) charge sector. Between the flat regions (e.g., in the case $B=1.1$ T) J increases rapidly. This is because as ϵ increases the singlet transitions to the (0,2) sector before the triplet, resulting in the DQD potential penalizing the triplet. The nearly constant value of J at large ϵ is essentially the exchange energy of a doubly occupied single dot with confinement energy E_0.

Increasing the magnetic field favors the higher angular momentum of the triplet state relative to the singlet. The magnetic field needed to invert the singlet and triplet levels is lower for (1,1) states than for (0,2) states, and this creates a negative-J dip in the J vs ϵ curve at intermediate magnetic field,[9] as shown in Fig. 3. Since the slope dJ/dB is larger for (0,2) states, at large enough magnetic field the dip disappears.

B. Noise-robust regimes

Given this general dependence of the exchange energy on interdot bias, three regimes can be identified which are relatively robust to ϵ noise: (I) at low ϵ, where the electrons are relatively isolated and $J \approx 0$; (II) at high ϵ, where the singlet and triplet are in the (0,2) charge sector; and (III) at a local minimum, present for certain finite magnetic fields, where the singlet and triplet are between the (1,1) and (0,2) charge sectors. Whether the J vs ϵ curve in these regions can be made flat enough to meet the stated requirements [Eq. (4) and (6)] is a central question we address in this work.

Let us write the ϵ dependence of J explicitly, $J=J(\epsilon)$, and define the average change in $J(\epsilon)$ when ϵ changes by $\Delta\epsilon$ around ϵ_0: $\Delta J(\epsilon_0,\Delta\epsilon) = \frac{1}{2}[|J(\epsilon_0+\Delta\epsilon)-J(\epsilon_0)|+|J(\epsilon_0)-J(\epsilon_0-\Delta\epsilon)|]$. Values of ϵ used as rotation gate operating points must satisfy two criteria. Using Eq. (5),

$$|J(\epsilon)| \leq J_{max}(\theta,\tau) \equiv \hbar|\theta|/\tau, \tag{7}$$

where, as previously, θ is the gate rotation angle and τ is gate time. Secondly, in order to satisfy Eq. (4), ϵ must also be chosen so that

$$\Delta\epsilon_{\text{ctl}} \leq \Delta\epsilon_{\text{target}} \equiv \max\left\{\Delta\epsilon: \left|\frac{\Delta J(\epsilon,\Delta\epsilon)}{J(\epsilon)}\right|^2 < P_{th}\right\}, \tag{8}$$

where $\Delta\epsilon_{\text{ctl}}$ is the bias uncertainty achievable by the controlling electronics. Given τ, θ, P_{th}, and ϵ, $\Delta\epsilon_{\text{target}}$ defines a target value of $\Delta\epsilon$ which must be met in order to ensure noise robustness. In the case of a no-op gate, Eq. (6) needs to be satisfied with J_0 equal to the exchange energy at and around the operating point, that is,

$$\max\{|J(\epsilon')|^2 : \epsilon' \in [\epsilon+\Delta\epsilon, \epsilon+\Delta\epsilon]\} \leq \hbar^2 P_{th}/\tau_0^2. \tag{9}$$

The quantity $\Delta\epsilon_{\text{target}}$ can be defined in this case as the maximum value of $\Delta\epsilon$ for which Eq. (9) is satisfied. Thus, for fixed P_{th}, $\Delta\epsilon_{\text{ctl}}$, θ, and τ, one simultaneously seeks large $\Delta\epsilon_{\text{target}}$ and small $|J|$.

1. Regimes I and II

In regimes (I) and (II), $\Delta\epsilon_{\text{target}}$ can be made arbitrarily large by increasing L or E_0, respectively. In both regimes, $\Delta J/J$ decreases as the dots become more isolated, and eventually Eq. (8) will be satisfied. In regime (I), $|J(\epsilon)|$ also decreases as the dots become more isolated so that at large enough L or E_0, Eq. (7) [or Eq. (9)] will be satisfied. In regime (II), J takes a (usually nonzero) value dependent on E_0 and B that can be made to satisfy Eq. (7). Thus, in regimes (I) and (II) one can theoretically satisfy Eqs. (7) and (8), or Eq. (9) in the case of a no-op gate, by forming two isolated one-electron dots or a single two-electron dot.

Consider the system given by $E_0=3$ meV, $L=60$ nm, and $B=1667$ mT. These parameters have been tuned within the range of physically reasonable values to result in an exchange curve with two relatively flat regions at low and high ϵ. This curve is shown in Fig. 4 along with additional curves generated by varying E_0, L, and B around the point $E_0=3$ meV, $L=60$ nm, and $B=1667$ mT.

At low-ϵ [regime (I)], $|J|<10^{-5}$ μeV over a 3 meV window around $\epsilon=0$. Using Eq. (9) we find that the total idle time τ_0 can be up to (65.8 μs)$\sqrt{P_{th}}$ (66 ns when $P_{th}=10^{-6}$), which is typically the time of many gate operations. On the high-ϵ flat (regime II), $J\approx 1$ μeV and $dJ/d\epsilon\approx 5\times 10^{-7}$. This allows rotation gate times of order 1 ns, and from Eq. (8) $\Delta\epsilon_{\text{target}}=(2\text{ eV})\sqrt{P_{th}}$ (2 meV for $P_{th}=10^{-6}$, which practically is limited by the width of the flat region). Although these results are only semiquantitative, and J could shift by several or tens of microelectron volt by using larger basis sizes, a small adjustment of the magnetic field could be used to counter this shift and tune the exchange curve back to essentially the one shown. This example shows that regimes exist for the DQD system where no-op and rotation operations are compatible with current quantum error correction and make realistic demands on controlling electronics technology. This statement assumes, however, that only ϵ noise is present (i.e., parameters L, B, and E_0 do not fluctuate).

In actuality, L, B, and E_0 cannot be perfectly controlled, and the variation in the exchange energy due to their fluctuations must be considered. In regime (I), when both the singlet and triplet are in the (1,1) charge sector, J is sensitive to the tunneling between the dots, and in general affected by L, E_0, and B. Because the exchange energy is suppressed with increasing tunnel barrier, however, J and its variation over a given L, E_0, or B interval can be made arbitrarily small by choosing sufficiently large L, E_0, and/or B. This is favorable for realizing a robust no-op. In the high-ϵ regime (II), both electrons are almost completely confined to a single dot, and J is strongly dependent on E_0 and B. The interdot spacing, on the other hand, has a relatively small effect on J that diminishes as ϵ increases. In general, similar qualitative behavior is obtained by increasing E_0 or increasing B (due to their common confining effect on the electrons). This gives some freedom in selecting a dot size (E_0), and involves inherent trade-offs. For instance, in large dots smaller magnetic fields can accomplish the same effects but larger dots are also more susceptible to disorder effects (e.g., phonon-induced spin-orbit coupling[21]).

The dependence of J on L, B, and E_0 in regimes (I) and (II) can be seen in Figs. 4(a), 4(c), and 4(e), respectively.

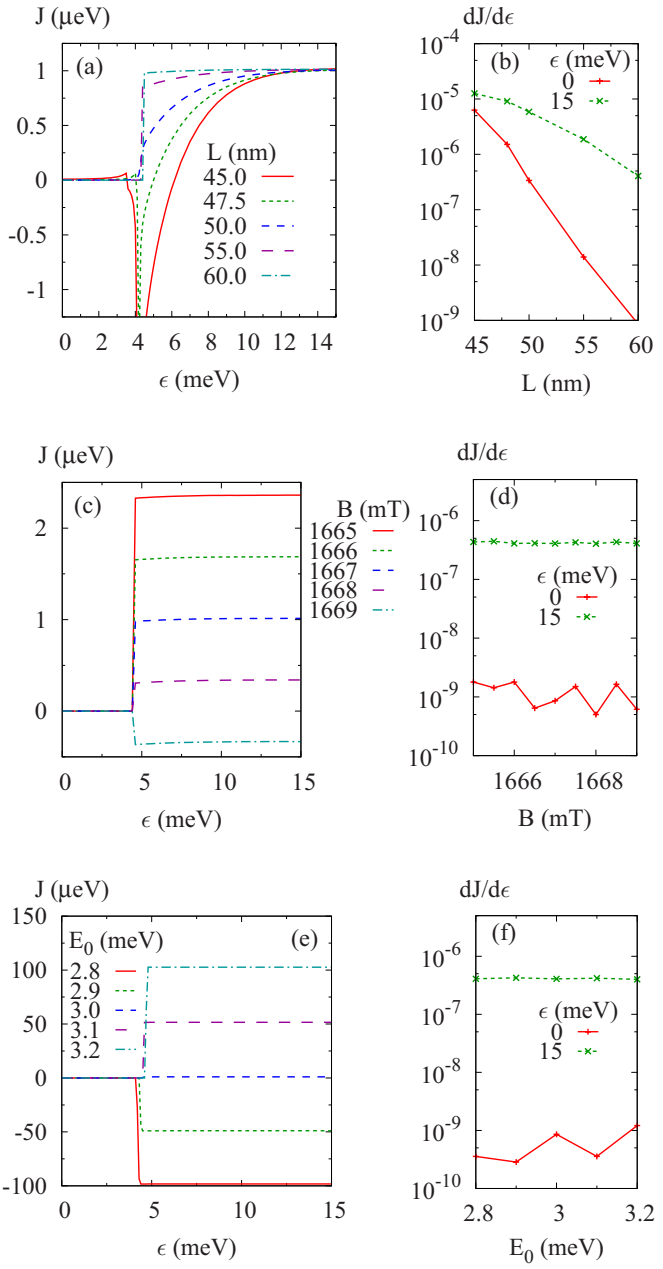

FIG. 4. (Color online) Trends in the flat regions [regimes (I) and (II) in text] of exchange energy vs bias curves around the point $E_0=3$ meV, $L=60$ nm, and $B=1667$ mT. Frames (a), (c), and (e) show the dependence on L (with $B=1667$ mT and $E_0=3$ meV), B (with $L=60$, and $E_0=3$ meV), and E_0 (with $L=60$ nm and $B=1667$ mT), respectively. Frames (b), (d), and (f) show the derivative $dJ/d\epsilon$ of the curve at their left for $\epsilon=0$ and 15 meV.

Additionally, Fig. 4(b) shows that the derivatives in these regimes are sensitive to L and therefore, even though changes in L do not affect the value of J on the upper flat, it must be sufficiently controlled that $dJ/d\epsilon$ remains within an acceptable range. Overall, to utilize the ϵ-noise robustness of regime (II) requires an ability to hold L, B, and E_0 fixed to the extent that Eq. (4) is satisfied. Variations in L are least problematic since keeping the dots sufficiently isolated will ensure that $dJ/d\epsilon$ is small. The typically strong linear depen-

dence of J on B and E_0, however, could not be avoided in the parameter ranges we studied.

In summary, if L, B, and E_0 can be held fixed precisely enough [i.e., to satisfy Eq. (4)], then there exist regimes of the DQD system which realize a robust no-op and rotation operation by varying only the interdot bias ϵ. These robust regimes meet the requirements for current quantum error correction architectures and the control of ϵ falls within current the capabilities of state-of-the-art electronics.

We note, however, that a large (0,2) singlet-triplet splitting is necessary for loading and measurement so that the singlet can be selected with high probability. Thus, if the high-ϵ regime is used for quantum operations, there must be a method of temporarily increasing the (0,2) exchange splitting during initialization and measurement.

2. Regime III

In regime (III), $dJ/d\epsilon=0$ exactly at the minimum, and it more informative to study the behavior of $\Delta\epsilon_{\text{target}}$ at the minimum, which is a measure of the curvature of $J(\epsilon)$ relative to its magnitude. For a given P_{th}, $\Delta\epsilon_{\text{target}}$ can be increased by decreasing B, L, or E_0. Decreasing B gives less energetic advantage to the triplet state (relative to the singlet) and results in the minimum becoming less sharp as well as occurring at smaller $|J|$, as shown in Fig. 5(a). Overall, $\Delta\epsilon_{\text{target}}$ increases as seen in Fig. 5(b). Either decreasing L or E_0 increases the overlap between (1,1) and (0,2) states. Even though this pushes the minimum to larger $|J|$ because the (1,1) states have greater (negative) exchange energy, $\Delta\epsilon_{\text{target}}$ increases because the (1,1)-(0,2) transitions of the singlet and triplet occur more gradually, and are farther separated in ϵ. This dependence on L is shown in Figs. 5(c) and 5(d), and the dependence on E_0 in Figs. 5(e) and 5(f). Note that in Fig. 5 we compensate an increase in E_0 by reducing B to obtain local minima which occur at similar values of J. Even without this compensation, lower values of E_0 give larger $\Delta\epsilon_{\text{target}}$ for fixed P_{th}. Because the singlet and triplet states have mixed (1,1) and (0,2) character in regime (III), variations in L, E_0, and B are particularly effective at changing the charge distribution of the singlet and triplet, and thereby the exchange energy. The sensitivity of J to variation in L is greater in this region than in either the low- or high-ϵ region, and the sensitivity to E_0 and B lies between that of the low- and high-ϵ regions.

Ideally, all three regimes could be used as robust operating points simultaneously with the low-ϵ region serving as an idle point. Multiple rotation speeds and negative rotation are potentially desirable for DCG. Achieving this goal is challenging for several reasons. The first is that broadening the regime-(III) minimum by coupling the dots more strongly is correlated with the exchange energy at $\epsilon=0$ increasing in magnitude (see Fig. 5). This sets up a competition between a robust idle state in regime (I) requiring small $|J|$, and a robust operating point in regime (III), which requires a broad minimum. Indeed, we find that for $P_{th}=10^{-4}$ and $\tau=1$ ns it is impossible to satisfy the constraints for an idle gate in regime (I) and a rotation gate in regime (III) at the same time. Secondly, achieving a given value of $|J|$ at large-ϵ requires tuning either the dot size (via E_0) or magnetic field. But since the magnetic field must be tuned to give a usable minimum in regime (III), tuning the dot size is necessary to simultaneously achieve a usable regime (II). For $|J|$ of order μeV these constraints can lead to very large dots (d greater than 200 nm). Figure 6 shows an example of a curve containing

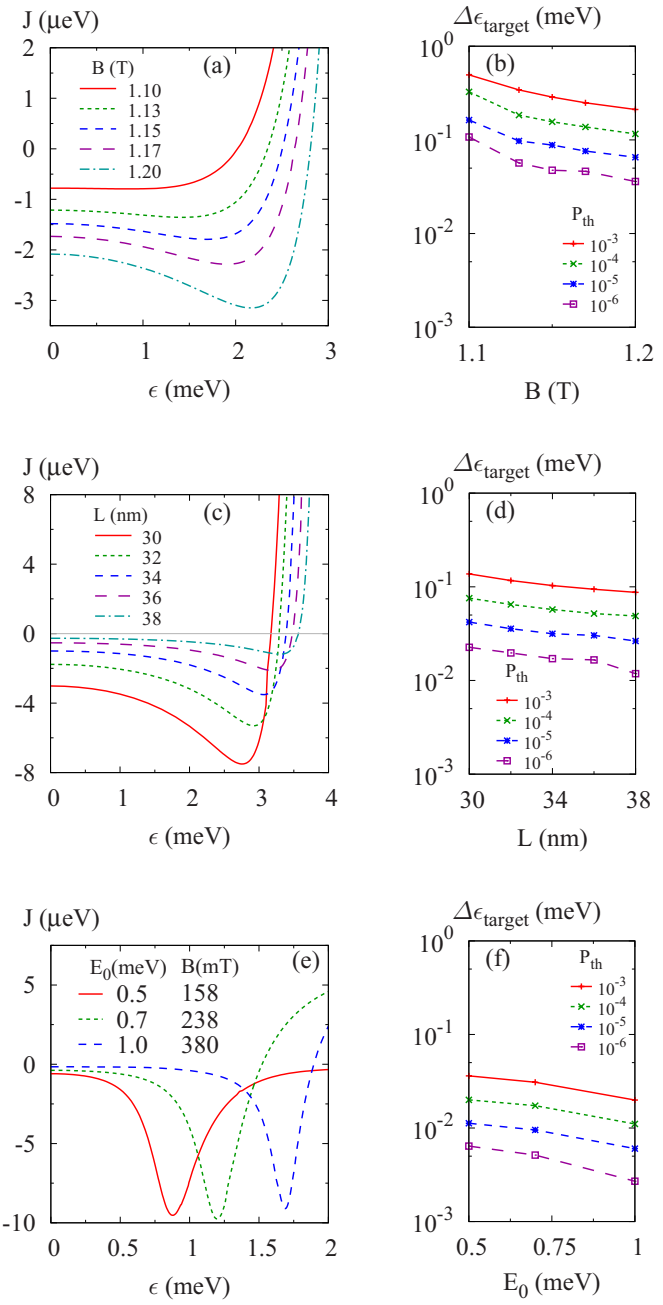

FIG. 5. (Color online) Trends in relative curvature around the local minimum in exchange energy as a function of DQD bias ϵ (regime II in text). Frames (a) and (b) show the dependence on B (with $L=30$, and $E_0=3$ meV) and L (with $B=1300$ mT and $E_0=3$ meV), respectively. Frames (c) and (d) plot the ratio $\Delta J/J$ as a function of B and L, respectively, for the plots in frames (a) and (c). It is seen that decreasing B or decreasing L correlates with smaller $\Delta J/J$, and this better robustness to ϵ variations. In frame (e), curves with $L=60$ nm and similar values at their minima, but different E_0, are shown, and it is seen that decreasing E_0 (and B) lead to greater ϵ robustness.

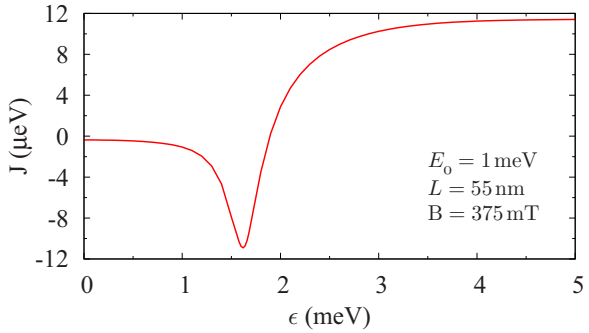

FIG. 6. (Color online) Exchange energy J vs. bias ϵ with three potential operating points lying at $\epsilon \approx 0$, 1.6, and 5 meV. To be compatible with an error threshold of 10^{-4}, however, would require a gate time of order 0.1 ns and control of ϵ to a few hundredths of a microelectronvolt.

operation points in all three regimes (and with regime I an idle point). Utilizing subsequent error correction, however, requires very fast gating of 0.1 ns and high detuning accuracy of 0.02 meV, which represents a significant technological challenge. Thus, we find that while the physics of the DQD system allows at least three robust operating points reachable by only changing the interdot bias, utilizing all three will require either finer electronics control or more efficient quantum error correction algorithms.

VI. DISCUSSION

A key observation from taking these results as a whole is that, while the DQD system offers some intrinsic robustness to certain types of noise, there is no ultimate "sweet spot" where the exchange energy is insensitive to all of the parameters involved. The fact that we have used a simple model should not weaken this statement, as adding more degrees of freedom will only provide additional paths for noise to perturb the system. We find, however, that advantage can be taken of DQD physics to eliminate sensitivity to a particular type of noise, and that if one knows what type of noise a particular device or system is most susceptible to, the operation of a DQD qubit can be tailored to combat this sensitivity. In the present work, we reduce the effect of interdot bias noise but still require fine control of other variables, such as the magnetic field.

We also fine (stated above) that realizing more than two operation points which are robust to noise in a single parameter is beyond current electronics capability. Here we note, however, that it may not be necessary to have three (or more) operating points separated only by changes in the interdot bias. One could envision implementing two rotation speeds in a DQD qubit by varying another parameter, such as E_0 or L, as well as ϵ, and to perform this alternate variation while $\epsilon = 0$ and the qubit is in a robust no-op state. Or perhaps only one rotation speed will be necessary to begin with. Our results indicate that a robust no-op should be accessible using current control and error correction technology, and that a robust rotation operation is also feasible as long as the shape of and spacing between the dots can be controlled with high precision.

Though dynamics are not studied in this work, it is important to realize that utilizing a (0,2)-flat region (regime II) requires the interdot bias to be quickly changed so that relatively little time is spent in the region of the J curve between the low- and high-ϵ flats. The speed at which this bias change occurs is limited by the gap to higher energy singlet and unpolarized triplet states as dictated by the adiabatic theorem. We have considered such restrictions, and find that the gap to excited levels remains large enough that the qubit can be moved adiabatically between regimes I and II with the vast majority of the gate time spent in the noise robust regimes. This does, however, set a bound on how weakly the dots can be coupled since the gap to excited states decreases with the interdot coupling.

The architecture of the DQD can be used to mitigate the effects of the exchange energy's sensitivity to L and E_0. To the extent that the actual DQD potential remains a double-parabolic well, there will be a mapping from sets of gate voltages to the parameters ϵ, L, and E_0. Variations in these parameters are thus determined by their dependence on the gate voltages which vary to perform a qubit operation. In this work, we have identified regions of (ϵ, L, E_0) space which are favorable for suppressing charge noise because they are flat, or nearly flat, along at least the ϵ direction. By modifying the architecture of a DQD device, one can hope to map the pathways in gate-voltage space that perform qubit operations onto pathways in (ϵ, L, E_0) space that begin and end along flat regions. In the present work, we specifically focus on robustness to ϵ variations, and the ideal architecture would allow gate voltages to change ϵ while keeping E_0 and L fixed. For example, to keep E_0 fixed for the right dot, changes in interdot bias might be controlled exclusively by varying the voltages of gates around the left dot. Such architecture engineering was first proposed by Friesen *et al.*,[16] where by moving the electrons along parallel channels instead of directly toward or away from each other, the interdot separation L varies only quadratically in the gate voltages at a finite-J operating point, instead of linearly. In that work, however, since the DQD is in a regime where J depended exponentially on L, the architecture serves only to reduce the sensitivity of L to the gate voltages, not to map the pathway onto a flat curve in (ϵ, L, E_0) parameter space.

VII. CONCLUSION

In summary, configuration interaction calculations on a singlet-triplet DQD qubit using GaAs material parameters have been carried out. Three regimes have been identified in which the exchange energy is relatively insensitive to changes in the interdot bias ϵ. The CI method is necessary to both qualitatively and quantitatively calculate the dependence of J on critical parameters such as detuning ϵ, dot energy E_0, and dot separation L, compared to more approximate schemes such as HL or HM. In particular, the CI method is found invaluable for calculations of critical regions such as when the dots are strongly coupled or when a single dot is doubly occupied. Namely, it captures the regime in which both the singlet and triplet transition into the (0,2) charge sector.

By tuning only the interdot bias, it is possible to travel between two or possibly three (with advances in electronics technology) of these robust regimes, which is desired for dynamically corrected gates and suggests how they might be implemented. These types of calculations are needed to provide guidance regarding accuracy requirements for ϵ, E_0, and L given a QEC threshold. We note the adverse effects caused by the sensitivity to certain parameters may be avoided by clever design of the qubit control electronics and architecture.

ACKNOWLEDGMENTS

We would like to thank Sankar Das Sarma, Mike Stopa, and Wayne Witzel for many helpful discussions during the preparation of this manuscript. This work was supported by the Laboratory Directed Research and Development program at Sandia National Laboratories. Sandia National Laboratories is a multiprogram laboratory operated by Sandia Corporation, a wholly owned subsidiary of Lockheed Martin company, for the U.S. Department of Energy's National Nuclear Security Administration under Contract No. DE-AC04-94AL85000.

APPENDIX A: MATRIX ELEMENTS BETWEEN *s*-TYPE GAUSSIAN FUNCTIONS

1. 1P Gaussian matrix elements

We derive here the matrix elements for single-particle operators which are piecewise polynomial in the components of particle position $\vec{r}$ and momentum $\vec{p}$. Since the basis functions are Gaussian, this reduces to the case of operators piecewise polynomial in the components of $\vec{r}$ ($\vec{p}=-i\hbar\nabla$ brings down powers of $\vec{r}$ from a Gaussian's exponent). Let us define two Gaussian basis elements, $|g_i\rangle$ and $|g_j\rangle$, by their real-space representations,

$$g_i(\vec{r}) = Ne^{-(\vec{r}-\vec{r}_A)\tilde{\alpha}(\vec{r}-\vec{r}_A)}, \quad g_j(\vec{r}) = N'e^{-(\vec{r}-\vec{r}_B)\tilde{\beta}(\vec{r}-\vec{r}_B)} \tag{A1}$$

In d dimensions, $\vec{r}_A$ and $\vec{r}_B$ are d-dimensional vectors which give the center positions of $|g_i\rangle$ and $|g_j\rangle$, and $\tilde{\alpha}$ and $\tilde{\beta}$ are $d\times d$ diagonal matrices specifying their exponential factors. We will make repeated use of the identity

$$g_i(\vec{r})g_j(\vec{r}) = NN'Ke^{-(\vec{r}-\vec{R}_{AB})\tilde{\mu}(\vec{r}-\vec{R}_{AB})}, \tag{A2}$$

where

$$K = e^{-(\vec{r}_A-\vec{r}_B)\tilde{C}(\vec{r}_A-\vec{r}_B)} \quad \text{with} \quad \tilde{C} = \tilde{\alpha}\tilde{\beta}/(\tilde{\alpha}+\tilde{\beta}), \tag{A3}$$

$$\vec{R}_{AB} = (\tilde{\alpha}\vec{r}_A + \tilde{\beta}\vec{r}_B)/(\tilde{\alpha}+\tilde{\beta}), \tag{A4}$$

$$\tilde{\mu} = \tilde{\alpha}+\tilde{\beta} \tag{A5}$$

which allows us to transform the product of two Gaussians into a single Gaussian. Throughout this appendix, division by a matrix means multiplication by its inverse.

Next, let us define a "piecewise-polynomial" operator $\mathcal{O}$ as one which can be written in the form

$$\mathcal{O} = \sum_i O_i(\vec{r})\chi_{[\vec{r}_i,\vec{r}_{i+1}]}(\vec{r}) \tag{A6}$$

$$= \sum_i \left(\sum_t^{N_i} c_t \prod_k^d r_k^{n(k,t)} \right) \chi_{[\vec{r}_i,\vec{r}_{i+1}]}(\vec{r}). \tag{A7}$$

O_i is polynomial in the components of $\vec{r}$ and is expanded in polynomial terms in the second line. The characteristic function $\chi_{[\vec{a},\vec{b}]}$ equals 1 within the d-dimensional interval $[\vec{a},\vec{b}]$ (e.g., a cube for $d=3$) and 0 everywhere else. The components of $\vec{a}$ and $\vec{b}$ are real or $\pm\infty$. Thus, $\langle g_i|\mathcal{O}|g_j\rangle$ is a linear combination of terms with the form $\langle g_i|\chi_{[\vec{a},\vec{b}]}(\vec{r})\Pi_{k=1}^d r_k^{n_k}|g_j\rangle$ where $\vec{n}$, $\vec{a}$, and $\vec{b}$ are d-dimensional vectors. We compute this general element immediately and then use the result to find the matrix elements of the kinetic and potential energy operators used for DQD Hamiltonians.

We begin the computation as follows:

$$\langle g_i|\chi_{[\vec{a},\vec{b}]}(\vec{r})\prod_{k=1}^d r_k^{n_k}|g_j\rangle = NN'K\int_{\vec{a}'}^{\vec{b}'} d^d\vec{u}e^{-\vec{u}\tilde{\mu}\vec{u}}\prod_{k=1}^d (u_k+R_{ABk})^{n_k} \tag{A8}$$

$$= NN'K\prod_{k=1}^d \int_{a_k'}^{b_k'} du_k e^{-\mu_{kk}u_k^2}(u_k+R_{ABk})^{n_k} \tag{A9}$$

$$= NN'K\prod_{k=1}^d \sum_{l=0}^{n_k} \binom{n_k}{l} (R_{ABk})^{n_k-l}\int_{a_k'}^{b_k'} du_k u_k^l e^{-\mu_{kk}u_k^2} \tag{A10}$$

$$= NN'K\prod_{k=1}^d \sum_{l=0}^{n_k} \binom{n_k}{l} (R_{ABk})^{n_k-l}F(l;a_k',b_k',\mu_{kk}). \tag{A11}$$

In the first line, we have used Eq. (A2) and made the substitution $\vec{u}=\vec{r}-\vec{R}_{AB}$. The limits of integration are from $\vec{a}'=\vec{a}-\vec{R}_{AB}$ to $\vec{b}'=\vec{b}-\vec{R}_{AB}$. In the second line, the integral written as product of one-dimensional integrals, and in the third line the binomial expansion of $(u_i+R_{ABi})^{n_i}$ is inserted. The fourth line [Eq. (A11)] defines the integral,

$$F(l;a,b,\mu) \equiv \int_a^b du u^l e^{-\mu u^2} \tag{A12}$$

which we now compute.

Using the shorthand notation $F(l)$ for $F(l;a,b,\mu)$,and integrating by parts [$U=u^{l-1}$, $dV=ue^{\mu u^2}du$, $dU=(l-1)u^{l-2}du$, $V=-1/(2\mu)e^{-\mu u^2}$],

$$F(l) = \left.\frac{-u^{l-1}}{2\mu}e^{-\mu u^2}\right]_a^b + \frac{l-1}{2\mu}\int_a^b u^{l-2}e^{-\mu u^2}du \tag{A13}$$

$$= G(l) + \frac{l-1}{2\mu} F(l-2) \quad \text{where} \quad G(l) \equiv \left. \frac{-u^{l-1}}{2\mu} e^{-\mu u^2} \right]_{u=a}^{b}. \tag{A14}$$

Since

$$F(0) = \int_a^b e^{-\mu u^2} du = \frac{1}{2}\sqrt{\frac{\pi}{\mu}} [\mathrm{erf}(\sqrt{\mu} b) - \mathrm{erf}(\sqrt{\mu} a)] \tag{A15}$$

and

$$F(1) = \int_a^b u e^{-\mu u^2} du = \frac{1}{2\mu} [e^{-\mu a^2} - e^{-\mu b^2}] \tag{A16}$$

can be computed directly, we can write $F(l)$ nonrecursively by

$$F(l) = \sum_{m=0}^{m_{max}} G(l-2m) \prod_{p=1}^{m} \frac{l-2p+1}{2\mu} + F^* \prod_{p=1}^{l/2} \frac{l-2p+1}{2\mu} \quad (l \text{ even}), \tag{A17}$$

where

$$m_{max} = \begin{cases} l/2-1 & l \text{ even} \\ (l-1)/2-1 & l \text{ odd} \end{cases} \quad \text{and} \quad F^* = \begin{cases} F(0) & l \text{ even} \\ F(1) & l \text{ odd}. \end{cases} \tag{A18}$$

In practice, $F(l)$ is calculated by a routine which iteratively builds the solution, such as the following (pseudo C++):

```
real F(k) {
  i=(k is even)?0:1
  x=F(i)
  while (i<k) {
    i++
    x*=i/(2*mu)
    i++
    x+=G(i)
  }
  return x
}
```

With the above analytic expression of $F(l;a,b,\mu)$, Eq. (A11) can be used to compute $\langle g_i|\chi_{[\vec{a},\vec{b}]}(\vec{r})\Pi_{k=1}^{d} r_k^{n_k}|g_j\rangle$ and thus the matrix elements of any piecewise-polynomial operator $\mathcal{O}$.

Note that if the matrix element is a single polynomial so that $a_k=-\infty$ and $b_k=+\infty$ for $k=1\ldots d$, then $F(l)$ is zero for odd l (integrand is odd) and for even l is given by the elementary integral,

$$\int_{-\infty}^{\infty} x^{2n} e^{-ax^2} dx = 2\sqrt{\pi} \frac{2n!}{n!} \left(\frac{1}{2\sqrt{a}}\right)^{2n+1}. \tag{A19}$$

Thus, in this simplified case when there are no characteristic functions,

$$\langle g_i|\prod_{k=1}^{d} r_k^{n_k}|g_j\rangle = NN' K \prod_{k=1}^{d} \left\{ \sum_{l=0,\text{even}}^{n_k} \binom{n_k}{l} \times (R_{ABk})^{n_k-l} \left[2\sqrt{\pi} \frac{l!}{(l/2)!} \left(\frac{1}{2\sqrt{\mu_{kk}}}\right)^{l+1} \right] \right\} \tag{A20}$$

Piecewise-polynomial potentials, such as parabolic or quartic quantum-dot potentials, are naturally expressed in the form given by Eq. (A6). Hamiltonian terms involving the momentum operator, however, require a few preliminary steps. For example, matrix elements of the kinetic-energy operator, $\langle g_i|-\nabla^2|g_j\rangle$, can written as matrix elements of the operator $(\vec{r}-\vec{r}_A)(4\tilde{\alpha}\tilde{\beta})(\vec{r}-\vec{r}_B)$, which is polynomial in $\vec{r}$ by integrating by parts and taking derivatives of the Gaussian basis functions,

$$\langle g_i| - \nabla^2|g_j\rangle = \int d^d\vec{r}\, \nabla \overline{g_i(\vec{r})} \cdot \nabla g_j(\vec{r}) \tag{A21}$$

$$= \int d^d\vec{r} \overline{g_i(\vec{r})} g_j(\vec{r})(\vec{r}-\vec{r}_A)(4\tilde{\alpha}\tilde{\beta})(\vec{r}-\vec{r}_B) \tag{A22}$$

$$= \langle g_i|(\vec{r}-\vec{r}_A)(4\tilde{\alpha}\tilde{\beta})(\vec{r}-\vec{r}_B)|g_j\rangle. \tag{A23}$$

Next define diagonal matrix $\tilde{P} \equiv \tilde{\alpha}\tilde{\beta}$, and use Eq. (A20) to arrive at a formula in terms of the basis element parameters,

$$\langle g_i| - \nabla^2|g_j\rangle = 4\langle g_i|\vec{r}\tilde{P}\vec{r} - \vec{r}\tilde{P}\vec{r}_B - \vec{r}_A\tilde{P}\vec{r} + \vec{r}_A\tilde{P}\vec{r}_B|g_j\rangle \tag{A24}$$

$$= 4NN' K \sum_{k}^{d} \left[P_{kk} \left(R_{ABk}^2 \sqrt{\frac{\pi}{\mu_{kk}}} + \frac{\sqrt{\pi}}{2\mu_{kk}^{3/2}} \right) \prod_{l\neq k} \sqrt{\frac{\pi}{\mu_{ll}}} \right. \tag{A25}$$

$$\left. + (r_{Ak}P_{kk}r_{Bk} - P_{kk}r_{Bk} - r_{Ak}P_{kk}) \prod_{l} \sqrt{\frac{\pi}{\mu_{ll}}} \right] \tag{A26}$$

$$= \mathcal{K} \sum_{k}^{d} P_{kk} \left[\frac{\sqrt{\pi}}{2\mu_{kk}^{3/2}} \prod_{l\neq k} \sqrt{\frac{\pi}{\mu_{ll}}} + (R_{ABk}^2 - (r_{Ak} + r_{Bk}) + r_{Ak}r_{Bk}) \prod_{l} \sqrt{\frac{\pi}{\mu_{ll}}} \right] \tag{A27}$$

$$= \mathcal{K} \sum_{k=1}^{d} P_{kk} \left(\frac{\sqrt{\pi}}{2\mu_{kk}^{3/2}} \right) \prod_{l\neq k} \sqrt{\frac{\pi}{\mu_{ll}}} + \vec{\Delta}_A \tilde{P} \vec{\Delta}_B \prod_{k=1}^{d} \sqrt{\frac{\pi}{\mu_{kk}}}. \tag{A28}$$

We define $\mathcal{K}=4NN'K$ in Eq. (A27), and in the last line we have defined $\vec{\Delta}_A \equiv \vec{R}_{AB} - \vec{r}_A$ and $\vec{\Delta}_B \equiv \vec{R}_{AB} - \vec{r}_B$.

The kinetic matrix element may also be computed directly as follows:

$$\langle g_i| - \nabla^2|g_j\rangle = \int d^d\vec{r}\, \nabla\, g_i(\vec{r}) \cdot \nabla g_j(\vec{r}) \tag{A29}$$

$$= 4NN' \int d^d\vec{r} e^{-(\vec{r}-\vec{r}_A)\tilde{\alpha}(\vec{r}-\vec{r}_A)} e^{-(\vec{r}-\vec{r}_B)\tilde{\alpha}(\vec{r}-\vec{r}_B)} (\vec{r}-\vec{r}_A)\tilde{P}(\vec{r}-\vec{r}_B) \tag{A30}$$

$$= \mathcal{K} \int d^d\vec{r} e^{-(\vec{r}-\vec{R}_{AB})\tilde{\mu}(\vec{r}-\vec{R}_{AB})} [(\vec{r}-\vec{R}_{AB}) + (\vec{R}_{AB}-\vec{r}_A)]\tilde{P}[(\vec{r}-\vec{R}_{AB}) + (\vec{R}_{AB}-\vec{r}_B)] \tag{A31}$$

$$= \mathcal{K} \int d^d\vec{u} e^{-\vec{u}\tilde{\mu}\vec{u}} \left[\vec{u}\tilde{P}\vec{u} + \vec{u}\tilde{P}\frac{\tilde{\alpha}-\tilde{\beta}}{\tilde{\alpha}+\tilde{\beta}}(\vec{r}_A-\vec{r}_B) + (\vec{R}_{AB}-\vec{r}_A)\tilde{P}(\vec{R}_{AB}-\vec{r}_B) \right] \tag{A32}$$

$$= \mathcal{K} \left[\int d^d\vec{u} e^{-\vec{u}\tilde{\mu}\vec{u}} \vec{u}\tilde{P}\vec{u} + \vec{\Delta}_A\tilde{P}\vec{\Delta}_B \int d^d\vec{u} e^{-\vec{u}\tilde{\mu}\vec{u}} \right] \tag{A33}$$

$$= \mathcal{K} \left[\sum_{i=1}^{d} \int d^d\vec{u} P_{ii} u_i^2 e^{-\vec{u}\tilde{\mu}\vec{u}} + \vec{\Delta}_A\tilde{P}\vec{\Delta}_B \int d^d\vec{u} e^{-\vec{u}\tilde{\mu}\vec{u}} \right] \tag{A34}$$

$$= \mathcal{K} \left[\sum_{i=1}^{d} P_{ii} \left(\int du_i u_i^2 e^{-\mu_{ii}u_i^2} \right) \left(\prod_{j\neq i} \int du_j e^{-\mu_{jj}u_j^2} \right) + \vec{\Delta}_A\tilde{P}\vec{\Delta}_B \prod_{i=1}^{d} \int du_i e^{-\mu_{ii}u_i^2} \right] \tag{A35}$$

$$= \mathcal{K} \left[\sum_{i=1}^{d} P_{ii} \left(\frac{\sqrt{\pi}}{2\mu_{ii}^{3/2}} \right) \prod_{j\neq i} \sqrt{\frac{\pi}{\mu_{jj}}} + \vec{\Delta}_A\tilde{P}\vec{\Delta}_B \prod_{i=1}^{d} \sqrt{\frac{\pi}{\mu_{ii}}} \right] \tag{A36}$$

We integrate by parts to get Eq. (A29), use Eq. (A2) to transition to Eq. (A31), and substitute $\vec{u}=\vec{r}-\vec{R}_{AB}$ in Eq. (A32). The term of Eq. (A32) linear in u vanishes since the integrand is odd. We then expand the matrix notation to arrive at Eq. (A35). The final line is obtained using the elementary integrals,

$$\int_{-\infty}^{\infty} e^{-ax^2} dx = \sqrt{\frac{\pi}{a}}, \tag{A37}$$

$$\int_{-\infty}^{\infty} x^2 e^{-ax^2} dx = \frac{\sqrt{\pi}}{2a^{3/2}}. \tag{A38}$$

The overlap matrix element can be calculated using Eq. (A11) and (A20), though it is straightforward to compute directly by using Eq. (A2) and the translation invariance of the integral. Following the latter approach, we obtain

$$\langle g_i | g_j \rangle = NN' \int d^d\vec{r} K e^{-\vec{r}\tilde{\mu}\vec{r}} = NN' K \sqrt{\frac{\pi^d}{\det \tilde{\mu}}}. \tag{A39}$$

2. Coulomb matrix elements

To compute the matrix elements of the m-body Hamiltonian (1) in the basis $\mathcal{B}_m^{\mathrm{MB}}$, matrix elements for the two-particle Coulomb term $\frac{e^2}{\kappa r}$ must be computed. We introduce two more Gaussian basis elements, $|g_{i'}\rangle$ and $|g_{j'}\rangle$ written similar to those in Eq. (A1),

$$g_{i'}(\vec{r}) = N'' e^{-(\vec{r}-\vec{r}_C)\tilde{\gamma}(\vec{r}-\vec{r}_C)}, \quad g_{j'}(\vec{r}) = N''' e^{-(\vec{r}-\vec{r}_D)\tilde{\delta}(\vec{r}-\vec{r}_D)}. \tag{A40}$$

Anticipating the combination of $g_{i'}(\vec{r})$ and $g_{j'}(\vec{r})$ using Eq. (A2), define the following analogous to Eqs. (A4) and (A5),

$$K' = e^{-(\vec{r}_C-\vec{r}_D)\tilde{C}(\vec{r}_C-\vec{r}_D)} \quad \text{with} \quad C = \tilde{\gamma}\tilde{\delta}/(\tilde{\gamma}+\tilde{\delta}), \tag{A41}$$

$$\vec{R}_{CD} = (\tilde{\gamma}\vec{r}_C + \tilde{\delta}\vec{r}_D)/(\tilde{\gamma}+\tilde{\delta}), \tag{A42}$$

$$\tilde{\nu} = \tilde{\gamma}+\tilde{\delta}. \tag{A43}$$

We now turn to the matrix element of interest. We begin by writing it as a real-space integral then apply Eq. (A2) to each pair of Gaussian basis elements,

$$\langle g_i g_{i'} | \frac{e^2}{\kappa r} | g_j g_{j'} \rangle = \frac{e^2}{\kappa} \int d^d\vec{r}_1 d^d\vec{r}_2 g_i(\vec{r}_1) g_{i'}(\vec{r}_2) \frac{1}{r_{12}} g_j(\vec{r}_1) g_{j'}(\vec{r}_2) \tag{A44}$$

$$= \mathcal{K} \frac{e^2}{\kappa} \int d^d\vec{r}_1 d^d\vec{r}_2 e^{-(\vec{r}_1-\vec{R}_{AB})\tilde{\mu}(\vec{r}_1-\vec{R}_{AB})} \frac{1}{r_{12}} e^{-(\vec{r}_2-\vec{R}_{CD})\tilde{\mu}(\vec{r}_2-\vec{R}_{CD})}, \tag{A45}$$

where $\mathcal{K} \equiv NN'N''N'''KK'$. Next, we write each of the two exponentials and $1/r_{12}$ in terms of their Fourier transforms, defined by $\mathrm{FT}[f(\vec{r})] = (2\pi)^{-d} \int d^d\vec{k} f(\vec{k}) e^{i\vec{k}\cdot\vec{r}}$. At this point we fix $d=3$ so that the Fourier transform of $1/r$ is well defined. The 2D solution will be obtained later, by taking a limit of the three-dimensional (3D) result. Thus, the Fourier transforms

$$\mathrm{FT}[e^{-\vec{x}\tilde{\alpha}\vec{x}}] = \left(\sqrt{\frac{\pi^d}{\det \tilde{\alpha}}} \right) e^{-1/4\vec{k}\tilde{\alpha}^{-1}\vec{k}} \tag{A46}$$

and

$$\mathrm{FT}\left[\frac{1}{r}\right] = \frac{4\pi}{k^2} \quad \text{for} \quad d=3 \tag{A47}$$

are inserted into in Eq. (A45) and result in (for $d=3$)

$$\langle g_i g_{i'} | \frac{e^2}{\kappa r} | g_j g_{j'} \rangle = \frac{\mathcal{K} e^2}{(2\pi)^{3d}\kappa} \int d^d\vec{r}_1 d^d\vec{r}_2 d^d\vec{k}_1 d^d\vec{k}_2 d^d\vec{k}_3 \sqrt{\frac{\pi^d}{\det \tilde{\mu}}} e^{-1/4\vec{k}_1\tilde{\mu}^{-1}\vec{k}_1} \tag{A48}$$

$$\times \frac{4\pi}{k_2^2}\sqrt{\frac{\pi^d}{\det\,\tilde{\nu}}}e^{-(1/4)\vec{k}_3\tilde{\nu}^{-1}\vec{k}_3}e^{i\vec{k}_1\cdot(\vec{r}_1-\vec{R}_{AB})}e^{i\vec{k}_2\cdot(\vec{r}_1-\vec{r}_2)}e^{i\vec{k}_3\cdot(\vec{r}_2-\vec{R}_{CD})}. \tag{A49}$$

Integrating over $\vec{r}_1$ and $\vec{r}_2$ yields delta functions $(2\pi)^d\delta(\vec{k}_1+\vec{k}_2)$ and $(2\pi)^d\delta(\vec{k}_2-\vec{k}_3)$. Then integrating over $\vec{k}_2$ and $\vec{k}_3$ effectively sets $-\vec{k}_1=\vec{k}_2=\vec{k}_3$ in the integrand, and we define $\vec{k}\equiv-\vec{k}_1$ to clean up the notation. After these integrations, Eq. (A49) becomes

$$\langle g_i g_{i'}|\frac{e^2}{\kappa r}|g_j g_{j'}\rangle = \frac{\mathcal{K}e^2}{(2\pi)^d\kappa}\frac{\pi^d}{\sqrt{\det\,\tilde{\mu}\tilde{\nu}}}\int d^d\vec{k}\frac{4\pi}{k^2}e^{-\vec{k}\tilde{\sigma}\vec{k}}e^{i\vec{k}\cdot\vec{\Delta}}, \tag{A50}$$

where $\tilde{\sigma}\equiv\frac{\tilde{\mu}+\tilde{\nu}}{4\tilde{\mu}\tilde{\nu}}$ (division is multiplication by matrix inverse) and $\vec{\Delta}=\vec{R}_{AB}-\vec{R}_{CD}$. Define $\sigma=\mathrm{Tr}(\tilde{\sigma})/d$, write $e^{-\vec{k}\tilde{\sigma}\vec{k}}=\exp(-\sigma k^2)\exp[-\vec{k}(\tilde{\sigma}-\sigma\mathbf{1})\vec{k}]$ ($\mathbf{1}$ is the identity matrix in d dimensions), and use the identity

$$\frac{e^{-\sigma k^2}}{k^2} = 2\sigma\int_0^1 dS S^{-3}e^{-\sigma k^2/S^2} \tag{A51}$$

(this follows from $e^{-a}=a\int_1^\infty e^{-ax}dx$ with $x=1/S^2$ and $a=\sigma k^2$) to transform Eq. (A50) into

$$\langle g_i g_{i'}|\frac{e^2}{\kappa r}|g_j g_{j'}\rangle = \frac{\mathcal{K}e^2}{\kappa}\frac{4\pi}{(2\pi)^d}\frac{\pi^d}{\sqrt{\det\,\tilde{\mu}\tilde{\nu}}}2\sigma\int_0^1\frac{dS}{S^3}\int d^d\vec{k}e^{-\vec{k}(\tilde{\sigma}-\sigma+\sigma/S^2)\vec{k}}e^{i\vec{k}\cdot\vec{\Delta}} \tag{A52}$$

$$= \frac{\mathcal{K}e^2}{\kappa}\frac{4\pi}{(2\pi)^d}\frac{\pi^d}{\sqrt{\det\,\tilde{\mu}\tilde{\nu}}}2\sigma\int_0^1\frac{dS}{S^3}\frac{\pi^{d/2}e^{-1/4\vec{\Delta}(\tilde{\sigma}-\sigma+\sigma/S^2)^{-1}\vec{\Delta}}}{\sqrt{\det(\tilde{\sigma}-\sigma+\sigma/S^2)}} \tag{A53}$$

$$= \frac{\mathcal{K}e^2}{\kappa}\frac{\pi^{d/2+1}\sigma}{2^{d-3}}(\det\,\tilde{\mu}\tilde{\nu})^{-1/2}I(\tilde{\sigma},\vec{\Delta}) \tag{A54}$$

$$= \frac{\mathcal{K}e^2}{\kappa}\pi^{5/2}\sigma(\det\,\tilde{\mu}\tilde{\nu})^{-1/2}I(\tilde{\sigma},\vec{\Delta}), \tag{A55}$$

where $\sigma\equiv\sigma\mathbf{1}$ when used in a matrix context, and in the last line we explicitly put $d=3$. In Eq. (A54), we have defined the integral

$$I(\tilde{\sigma},\vec{\Delta}) = \int_0^1\frac{dS}{S^3}[\det(\tilde{\sigma}-\sigma+\sigma/S^2)]^{-1/2}e^{-1/4\vec{\Delta}(\tilde{\sigma}-\sigma+\sigma/S^2)^{-1}\vec{\Delta}} \tag{A56}$$

$$= \int_0^1\frac{dS}{S^3}\left[\prod_{i=1}^3(\sigma_{ii}-\sigma(1-1/S^2))\right]^{-1/2}e^{-1/4\Sigma_{i=1}^3\vec{\Delta}_i^2/(\sigma_{ii}-\sigma(1-1/S^2))}. \tag{A57}$$

The second line follows since $\tilde{\sigma}$ is a 3×3 diagonal matrix. We cannot express the integral in closed form, and so must compute $I(\tilde{\sigma},\vec{\Delta})$ numerically. In the two-dimensional case, we take the limit $\mu_{33}=\nu_{33}\to\infty$, which means that $\sigma_{33}\to0$. This is the limit where all the Gaussian basis elements have the same width η in the z direction, and η approaches zero (making the elements two dimensional). $\mathcal{K}$ contains the factor $(2\alpha_{33}/\pi)^{1/4}(2\beta_{33}/\pi)^{1/4}(2\gamma_{33}/\pi)^{1/4}(2\delta_{33}/\pi)^{1/4}=2\eta/\pi$, which cancels the factor $1/\sqrt{\mu_{33}\nu_{33}}=1/\sqrt{(2\eta)(2\eta)}=1/(2\eta)$ from $(\det\,\tilde{\mu}\tilde{\nu})^{-1/2}$, leaving a factor of π in the denominator. This reduces the exponent of π in Eq. (A55) from 5/2 to 3/2 as seen below in Eq. (A59).

The integral $I(\tilde{\sigma},\vec{\Delta})$ converges. The only possible trouble occurs when $[\sigma_{ii}-\sigma(1-1/S^2)]=0$, or equivalently $S=1/\sqrt{1-\sigma_{ii}/\sigma}$, for some $i=1,2,3$. Since $\sigma_{ii}>0$ implies that $1/\sqrt{1-\sigma_{ii}/\sigma}$ is either imaginary or greater than 1, the only divergence of the integrand for $S\in[0,1]$ occurs at $S=1$ when $\sigma_{ii}=0$. Although this happens for $i=3$ in the 2D case ($\sigma_{33}=0$), the divergence is $\sim1/\sqrt{1-S}$, which is integrable. Thus, the integral is well defined and convergent over the entire range of physical parameters.

In summary, the Coulomb term matrix elements for two and three dimensions can be carried out analytically up to the numerical evaluation of a convergent one-dimensional integral. They are given by

$$\langle g_i g_{i'}|\frac{e^2}{\kappa r}|g_j g_{j'}\rangle = \frac{\mathcal{K}e^2}{\kappa}\pi^{5/2}\sigma(\det\,\tilde{\mu}\tilde{\nu})^{-1/2}I(\tilde{\sigma},\vec{\Delta}) \quad \text{(3D)}, \tag{A58}$$

$$\langle g_i g_{i'}|\frac{e^2}{\kappa r}|g_j g_{j'}\rangle = \frac{\mathcal{K}_{2D}e^2}{\kappa}\pi^{3/2}\sigma(\det_{2D}\,\tilde{\mu}\tilde{\nu})^{-1/2}I(\tilde{\sigma},\vec{\Delta}) \quad \text{(2D)}. \tag{A59}$$

The subscripts "2D" are a reminder that the normalization factors and determinant contain only x and y factors.

3. Implementation note

We note additionally that when the integral for two dimensions is computed numerically, the integral around $S=1$ is approximated by a closed form. At $S=1-\epsilon$, when $\epsilon\ll1$, the integrand in Eq. (A56), which we denote $W(S)$, is approximated via the expansion

$$\tilde{\sigma}-\sigma\left(1-\frac{1}{(1-\epsilon)^2}\right)\approx\tilde{\sigma}+2\sigma\epsilon \tag{A60}$$

resulting in an approximation for the integral between $S=1-\epsilon_0$ and 1,

$$\int_{1-\epsilon}^1 dS W(S) \approx \int_{1-\epsilon}^1 dS\,\det[\tilde{\sigma}+\sigma(2\epsilon)]^{-1/2}(1-\epsilon)^{-3}e^{-1/4(\Delta_x^2\sigma_x^{-1}+\Delta_y^2\sigma_y^{-1})} \tag{A61}$$

$$= \int_0^{\epsilon_0} d\epsilon[\sigma_x\sigma_y\sigma(2\epsilon)]^{-1/2}e^{-1/4(\Delta_x^2\sigma_x^{-1}+\Delta_y^2\sigma_y^{-1})} \tag{A62}$$

$$= \frac{e^{-1/4(\Delta_x^2\sigma_x^{-1}+\Delta_y^2\sigma_y^{-1})}}{\sqrt{2\sigma_x\sigma_y\sigma}} \int_0^{\epsilon_0} \frac{d\epsilon}{\sqrt{\epsilon}} \tag{A63}$$

$$= \frac{\sqrt{2\epsilon_0}e^{-1/4(\Delta_x^2\sigma_x^{-1}+\Delta_y^2\sigma_y^{-1})}}{\sqrt{\sigma_x\sigma_y\sigma}}. \tag{A64}$$

4. Isotropic Gaussian functions—the completely analytic case

When all the Gaussian basis elements are isotropic, that is, when $\tilde{\alpha}$ is a proportional to the identity, then Coulomb matrix elements can be computed analytically in both two and three dimensions. In 3D, we follow the above derivation up to Eq. (A50) and let $\tilde{\mu}=\mu\mathbf{1}$, $\tilde{\nu}=\nu\mathbf{1}$, and $\tilde{\sigma}=\sigma\mathbf{1}$ define the scalars μ, ν, and σ corresponding to the similarly named matrix. Then write Eq. (A50) in spherical coordinates with the z axis along $\vec{\Delta}$ to obtain

$$\langle g_i g_{i'}|\frac{e^2}{\kappa r}|g_j g_{j'}\rangle = \mathcal{K}' \int k^2 dk d(\cos\theta) d\phi \frac{4\pi}{k^2} e^{-\sigma k^2} e^{ik\Delta\cos\theta} \tag{A65}$$

$$= 4\pi\mathcal{K}' \int_0^\infty dk e^{-\sigma k^2} \int_{-1}^1 d(\cos\theta) e^{ik\Delta\cos\theta} \int_0^{2\pi} d\phi \tag{A66}$$

$$= 8\pi^2\mathcal{K}' \int_0^\infty dk \frac{e^{-\sigma k^2}}{ik\Delta}(e^{ik\Delta} - e^{-ik\Delta}) \tag{A67}$$

$$= 16\pi^2\mathcal{K}' \int_0^\infty dk e^{-\sigma k^2} \frac{\sin k\Delta}{k\Delta} \tag{A68}$$

$$= \frac{16\pi^2\mathcal{K}'}{\Delta} \int_0^\Delta dy \int_0^\infty dk e^{-\sigma k^2} \cos ky \tag{A69}$$

$$= \frac{8\pi^2\mathcal{K}'}{\Delta} \int_0^\Delta dy \int_{-\infty}^\infty dk e^{-\sigma k^2} \cos ky, \tag{A70}$$

where $\mathcal{K}'=\frac{\mathcal{K}e^2}{8\kappa}(\mu\nu)^{-3/2}$. In line Eq. (A69), we introduce a dummy variable y in order to make the k-integral tractable (see below). The final line uses the fact that the integrand is even to extend the range of integration. By writing $\cos ky$ in exponential form and completing the squares, we can integrate over k to get,

$$\langle g_i g_{i'}|\frac{e^2}{\kappa r}|g_j g_{j'}\rangle = \frac{4\pi^2\mathcal{K}'}{\Delta} \int_0^\Delta dy \int_{-\infty}^\infty dk e^{-\sigma k^2}(e^{iky} + e^{-iky}) \tag{A71}$$

$$= \frac{4\pi^2\mathcal{K}'}{\Delta} \int_0^\Delta dy \int_{-\infty}^\infty dk (e^{-\sigma(k - iy/2\sigma)^2} + e^{-\sigma(k + iy/2\sigma)^2}) e^{-y^2/4\sigma} \tag{A72}$$

$$= \frac{4\pi^2\mathcal{K}'}{\Delta} \int_0^\Delta dy \int_{-\infty}^\infty dk 2e^{-\sigma k^2} e^{-y^2/4\sigma} \tag{A73}$$

$$= \frac{8\pi^2\mathcal{K}'}{\Delta} \sqrt{\frac{\pi}{\sigma}} \int_0^\Delta dy e^{-y^2/4\sigma} \tag{A74}$$

$$= \frac{8\pi^2\mathcal{K}'}{\Delta} \sqrt{\frac{\pi}{\sigma}} \left[\frac{\sqrt{\pi/(4\sigma)}}{2} \mathrm{erf}(\Delta\sqrt{4\sigma}) \right] \tag{A75}$$

$$= \mathcal{K}' \frac{2\pi^3}{\sigma} \frac{\mathrm{erf}(\Delta\sqrt{4\sigma})}{\Delta}. \tag{A76}$$

We obtain line (A73) by shifting k in each of the terms (in different directions), which does not alter the integral and introduce the error function $\mathrm{erf}(x)=\frac{2}{\sqrt{\pi}}\int_0^x dx' e^{-x'^2}$ on line (A75). Expanding $\mathcal{K}'$ gives us a final analytic formula for Coulomb matrix elements in three dimensions ($d=3$),

$$\langle g_i g_{i'}|\frac{e^2}{\kappa r}|g_j g_{j'}\rangle = \frac{\mathcal{K}e^2}{4\kappa\sigma} \frac{\pi^3}{(\mu\nu)^{3/2}} \frac{\mathrm{erf}(\Delta\sqrt{4\sigma})}{\Delta} \quad (3\mathrm{D, isotropic}). \tag{A77}$$

In 2D, we proceed to Eq. (A45) as above, but then insert 2D Fourier transforms instead of the 3D ones yielding Eq. (A49). The Fourier transform of the Gaussian basis elements has the same form as the 3D case but now

$$\mathrm{FT}\left[\frac{1}{r}\right] = \frac{2\pi}{k} \quad \text{for} \quad d=2. \tag{A78}$$

Inserting these into to Eq. (A45) (with $d=2$) gives

$$\langle g_i g_{i'}|\frac{e^2}{\kappa r}|g_j g_{j'}\rangle = \frac{\mathcal{K}e^2}{(2\pi)^6\kappa} \int d^2\vec{r}_1 d^2\vec{r}_2 d^2\vec{k}_1 d^2\vec{k}_2 d^2\vec{k}_3 \sqrt{\frac{\pi^2}{\mu^2}} e^{-k_1^2/(4\mu)} \tag{A79}$$

$$\times \frac{2\pi}{k_2} \sqrt{\frac{\pi^2}{\nu^2}} e^{-k_3^2/(4\nu)} e^{i\vec{k}_1\cdot(\vec{r}_1-\vec{R}_{AB})} e^{i\vec{k}_2\cdot(\vec{r}_1-\vec{r}_2)} e^{i\vec{k}_3\cdot(\vec{r}_2-\vec{R}_{CD})}. \tag{A80}$$

As in the 3D case, integrating over $\vec{r}_1$ and $\vec{r}_2$ produces delta functions which are removed by then integrating over $\vec{k}_2$ and $\vec{k}_3$. This effectively sets $\vec{k}\equiv-\vec{k}_1=\vec{k}_2=\vec{k}_3$ in the integrand,

$$\langle g_i g_{i'}|\frac{e^2}{\kappa r}|g_j g_{j'}\rangle = \frac{\mathcal{K}e^2}{4\kappa} \frac{1}{\mu\nu} \int d^2\vec{k} \frac{2\pi}{k} e^{-\sigma k^2} e^{i\vec{k}\cdot\vec{\Delta}}, \tag{A81}$$

where $\sigma\equiv\frac{\mu+\nu}{4\mu\nu}$ and $\vec{\Delta}=\vec{R}_{AB}-\vec{R}_{CD}$. Again we use the scalars μ, ν, and σ which correspond to matrices in the more general (nonisotropic) case. Changing to polar coordinates with the x axis along $\vec{\Delta}$,

$$\langle g_i g_{i'} | \frac{e^2}{\kappa r} | g_j g_{j'} \rangle = \frac{\mathcal{K} e^2}{2\kappa} \frac{\pi}{\mu\nu} \int_0^{\pi} d\theta \int_{-\infty}^{\infty} dk e^{-\sigma k^2} e^{ik\Delta \cos\theta} \tag{A82}$$

$$= \frac{\mathcal{K} e^2}{2\kappa} \frac{\pi}{\mu\nu} \int_0^{\pi} d\theta \int_{-\infty}^{\infty} dk e^{-\sigma(\vec{k} - i\vec{\Delta} \cos\theta/2\sigma)^2} e^{-\Delta^2 \cos^2\theta/4\sigma} \tag{A83}$$

$$= \frac{\mathcal{K} e^2}{2\kappa} \frac{\pi}{\mu\nu} \int_0^{\pi} d\theta \left[\int_{-\infty}^{\infty} dk e^{-\sigma(\vec{k} - i\vec{\Delta} \cos\theta/2\sigma)^2} \right] \times e^{-\Delta^2/(8\sigma)} e^{-\Delta^2 \cos 2\theta/8\sigma} \tag{A84}$$

$$= \frac{\mathcal{K} e^2}{2\kappa} \frac{\pi}{\mu\nu} \sqrt{\frac{\pi}{\sigma}} e^{-\Delta^2/(8\sigma)} \left(\frac{1}{2} \int_0^{2\pi} d\theta' e^{-\Delta^2/(8\sigma)\cos\theta'} \right) \tag{A85}$$

$$= \frac{\mathcal{K} e^2}{2\kappa} \frac{\pi^2}{\mu\nu} \sqrt{\frac{\pi}{\sigma}} e^{-\Delta^2/(8\sigma)} I_0\left(\frac{-\Delta^2}{8\sigma} \right). \tag{A86}$$

On line (A83) we have completed the square, and to obtain line (A84) the trigonometric identity $\cos^2\theta = (1+\cos 2\theta)/2$ is used. The quantity in square brackets on line (A84) is equal to $\sqrt{\pi/\sigma}$ (the variable in integration can be shifted). The parenthesized quantity on line (A85) is equal to $\int_0^{\pi} d\theta' \exp[-(\Delta^2/8\sigma)\cos\theta']$ by symmetry, which is equal to $\pi I_0[-\Delta^2/(8\sigma)]$, where I_0 is the first modified Bessel function. Combining terms, we arrive at a final analytic formula for Coulomb matrix elements in 2D,

$$\langle g_i g_{i'} | \frac{e^2}{\kappa r} | g_j g_{j'} \rangle = \frac{\mathcal{K} e^2}{2\kappa\sqrt{\sigma}} \frac{\pi^{5/2}}{\mu\nu} e^{-\Delta^2/(8\sigma)} I_0\left(\frac{-\Delta^2}{8\sigma} \right) \quad \text{(2D,isotropic)}. \tag{A87}$$

APPENDIX B: OPTIMIZATION OF GAUSSIAN FUNCTION PARAMETERS

The computational speed of the configuration interaction method described in these notes is dependent on its ability to use relatively small basis sizes (i.e., numbers of Gaussian elements) to obtain semiquantitative results. To achieve a more rapid convergence with respect to the basis size, the placement and exponential factor of the Gaussian basis elements is optimized within a subspace of all possible sets. This optimization process is of great practical importance since results must converge before reaching the maximum n_G allowed by our computational resources (currently 50–100). In this section, we explain in detail the method used to choose an "optimal" set of Gaussian basis functions.

The number of basis elements n_G is always given as a fixed parameter to the optimization procedure. An initial basis of n_G elements is generated by specifying either (I) the location and size of each dot, along with and the number of elements to place in it, or (II) the location (in a 2D plane) and size of each Gaussian function. Method (I) requires that the system be comprised of one or more quantum dots, where method (II) can be used for any system.

Positions of the elements in a Gaussian basis are generated from an underlying two-dimensional mesh of points with two characteristic length scales a_x and a_y (usually the spacing between elements associated with the same quantum dot along the x and y axis, respectively). Method (I) creates this mesh based on location and size of the dots, and always places a mesh point at the center of each dot. In method (II), the locations of elements are given in terms of a_x and a_y, which are given separately.

The elements in a basis are partitioned into n_{SS} subsets such that the exponential factor [the diagonal matrix $\tilde{\alpha}$ in Eq. (A1)] is the same for elements in the same subset. Initial values for the exponential factors, denoted $\tilde{\alpha}_i$ for $i=1\ldots n_{SS}$, are either chosen based on the dot size (method I) or specified directly (method II). The point of these subsets is to reduce the number of independent parameters needed to optimize, as each of these "subset-wide" exponential-factor values (not each element's factor independently) is found by optimization. If the Gaussian elements are required to be isotropic, each $\tilde{\alpha}$ must be a multiple of the identity. This restriction results in less freedom for basis optimization but increased computation speed. In the case of method I, $n_{SS}=2$, and the elements at the center of each dot are allowed to have a different exponential factor than the rest of the elements. When there are multiple basis elements at a given mesh point the exponential factors of additional elements are found by multiplying the previous element's coefficient by a constant factor λ. Method I fixes $\lambda=1.5$ and method II takes a value for λ as input.

Optimization of the basis is performed by multidimensional minimization of an energy E with respect to a_x, a_y, α_i,

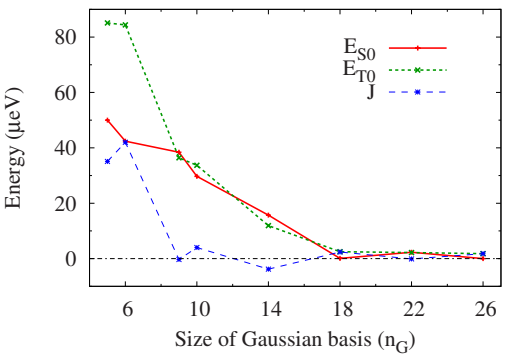

n_G	Fig.8
5	A
6	A*
9	B
10	B*
14	C*
18	B+B
22	B+C
26	B+D

FIG. 7. (Color online) The CI-computed lowest-lying singlet (E_{S0}) and triplet (E_{T0}) energies *relative to the exact value* as a function of basis size. Their difference, the exchange energy $J=E_{T0}-E_{S0}$ is also given relative to the exact value. The spatial arrangement of the basis elements for each size is given in the table to the right, which gives a letter A-D of a spatial plot in Fig. 8. A trailing asterisk (*) indicates that there are two basis elements lying on top of one another at the center of the dot, and the sum (+) of two letters indicates that the elements of the referred to spatial plots are combined (elements at the same position have different exponential factors). Dot parameters $\hbar\omega_0=3$ meV and $B=0$.

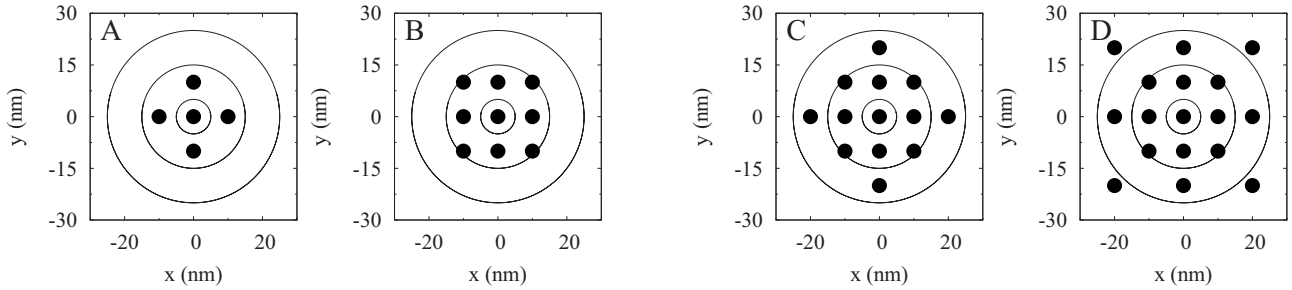

FIG. 8. Spatial arrangements of Gaussian basis elements in a single quantum dot. Each solid black circle represents at least one basis element. There can be more than one element at a given point (circle) as specified by the table in Fig. 7. Note that these diagrams only describe the relative arrangement of the Gaussian centers; the "grid spacing" of the centers is optimized.

and λ simultaneously. The energy minimized is the either (1) the lowest single-electron energy, (2) the lowest many-body energy, or (3) the lowest many-body energy with a given symmetry (e.g., $S_z=0$ and total spin $S=1$). In the case when multiple eigenstates with different symmetry are required the minimization is done multiple times, once for each symmetry. In the results for the exchange energy presented in this work we perform minization via case (3) twice: once to minimize the lowest singlet energy and once to minimize the lowest unpolarized triplet energy. Their difference is the reported exchange energy.

APPENDIX C: COMPARISON OF THE CI IN AN EXACTLY SOLVABLE CASE: SINGLE PARABOLIC DOT

In this appendix, we compute the energies of a single parabolic quantum dot in two dimensions using the full CI method presented in this paper. With two interacting electrons, the system energies can be found exactly (the computation can be done analytically for certain dot confinement energies and numerically for any set of parameters using a one-dimensional Schrodinger solver).[22] Comparison with this exact solution provides a useful benchmark for the CI, and we are able to analyze how well a Gaussian basis is able to capture a strongly correlated two-electron state. By varying the basis size, information on the convergence of the CI is obtained. As a side remark, we note that the CI will always find the correct single-electron ground state energy since one of the Gaussian basis elements is chosen to be exactly this solution.

Consider a single parabolic dot, given by the potential

$$V(\vec{r}) = \frac{1}{2} m^* \omega_0^2 r^2, \tag{C1}$$

where m^* is the effective mass and $\hbar\omega_0$ is the confinement energy of the dot. We insert this potential into Eq. (1) where $n=2$ is the number of electrons (there is no Coulomb repulsion term when $n=1$). We use GaAs material parameters: $\kappa = 12.9$, and $m^*=0.067m_e$.

We solve the full Hamiltonian exactly using the method in Ref. 22 to reduce the problem to an ordinary (one-dimensional) Schrodinger equation by switching to center of mass coordinates. We then solve this equation using the technique prescribed in Ref. 23. The lowest singlet (total spin $S=0$) and unpolarized triplet ($S=1, S_z=0$) energies obtained by the CI relative to the exact solution are shown in Fig. 7 as a function of basis size. As size does not uniquely specify a basis, we give the spatial arrangement of the basis elements used in Fig. 8 which is referenced by the table in in Fig. 7. Overall, we find for a range of dot confinement ω_0 and magnetic field B that the CI energies converge to within ≈0.5% of their value for basis sizes around 10, and to within ≈0.05% for basis sizes around 20. Thus, for the dot parameters of Fig. 7 where the energies are of order 10 meV, convergence is obtained to within 50 and 5 μeV for roughly 10 and 20 basis elements, respectively. This assumes a good basis arrangement (cf. Fig. 8), as a poor choice of where to place the basis elements (e.g., all in a single line) will clearly not produce converged values even for large basis sizes.

[1] J. Levy, Phys. Rev. Lett. **89**, 147902 (2002).
[2] G. Burkard, D. Loss, and D. P. DiVincenzo, Phys. Rev. B **59**, 2070 (1999).
[3] B. E. Kane, Nature (London) **393**, 133 (1998).
[4] J. M. Taylor H.-A. Engel, W. DāR, A. Yacoby, C. M. Marcus, P. Zoller, and M. D. Lukin, Nat. Phys. **1**, 177 (2005).
[5] J. Petta, A. Johnson, J. Taylor, E. Laird, A. Yacoby, M. Lukin, C. Marcus, M. Hanson, and A. Gossard, Science **309**, 2180 (2005).
[6] M. A. Nielsen and I. L. Chuang, *Quantum Computation and Information* (Cambridge University Press, Cambridge, England, 2000).
[7] E. Knill and R. Laflamme, Phys. Rev. A **55**, 900 (1997).
[8] J. Levy, A. Ganti, C. Phillips, B. Hamlet, A. Landahl, T. Gurrieri, R. Carr, and M. Carroll, arXiv:0904.0003 (unpublished).
[9] M. Stopa and C. M. Marcus, Nano Lett. **8**, 1778 (2008).
[10] K. Khodjasteh and L. Viola, Phys. Rev. A **80**, 032314 (2009).
[11] A. Szabo and N. S. Ostlund, *Modern Quantum Chemistry: Introduction to Advanced Electronic Structure Theory* (Dover, New York, 1996).
[12] P. Schmelcher, M. V. Ivanov, and W. Becken, Phys. Rev. A **59**,

3424 (1999).
[13] M. Rontani, C. Cavazzoni, D. Bellucci, and G. Goldoni, J. Chem. Phys. **124**, 124102 (2006).
[14] T. Sako and G. H. F. Diercksen, Phys. Rev. B **75**, 115413 (2007).
[15] T. Chwiej and B. Szafran, Phys. Rev. B **78**, 245306 (2008).
[16] M. Friesen, R. Joynt, and M. A. Eriksson, Appl. Phys. Lett. **81**, 4619 (2002).
[17] M. J. Calderón, B. Koiller, and S. Das Sarma, Phys. Rev. B **74**, 045310 (2006).
[18] J. Pedersen, C. Flindt, N. A. Mortensen, and A.-P. Jauho, Phys. Rev. B **76**, 125323 (2007).
[19] S. R. Ekanayake, T. Lehmann, A. S. Dzurak, and R. G. Clark, *Nanotechnology, 2008* (NANO '08. 8th IEEE Conference), 18–21 August 2008, Arlington, TX, pp. 472–475.
[20] K. Khodjasteh, D. Lidar, and L. Viola, Phys. Rev. Lett. **104**, 090501 (2010).
[21] S. Amasha, K. MacLean, I. P. Radu, D. M. Zumbuhl, M. A. Kastner, M. P. Hanson, and A. C. Gossard, Phys. Rev. Lett. **100**, 046803 (2008).
[22] M. Taut and H. Eschrig, arXiv:0911.2400 (unpublished).
[23] I. W. Sudiarta and D. J. W. Geldart, J. Phys. A: Math. Theor. **40**, 1885 (2007).